# Real-space visualization of a defect-mediated charge density wave transition

James L. Hart<sup>a,1</sup>, Haining Pan<sup>b,1</sup>, Saif Siddique<sup>a</sup>, Noah Schnitzer<sup>a</sup>, Krishnanand Mallayya<sup>b</sup>, Shiyu Xu<sup>a</sup>, Lena F. Kourkoutis<sup>c,d</sup>, Eun-ah Kim<sup>b,e</sup>, and Judy J. Cha<sup>a,2</sup>

Affiliations are included on p. 6

Edited by Angel Rubio, Max-Planck-Institut fur Struktur und Dynamik der Materie, Hamburg, Germany; received January 30, 2024; accepted June 14, 2024

We study the coupled charge density wave (CDW) and insulator-to-metal transitions in the 2D quantum material 1T-TaS<sub>2</sub>. By applying in situ cryogenic 4D scanning transmission electron microscopy with in situ electrical resistance measurements, we directly visualize the CDW transition and establish that the transition is mediated by basal dislocations (stacking solitons). We find that dislocations can both nucleate and pin the transition and locally alter the transition temperature  $T_c$  by nearly ~75 K. This finding was enabled by the application of unsupervised machine learning to cluster five-dimensional, terabyte scale datasets, which demonstrate a one-to-one correlation between resistance—a global property—and local CDW domain-dislocation dynamics, thereby linking the material microstructure to device properties. This work represents a major step toward defect-engineering of quantum materials, which will become increasingly important as we aim to utilize such materials in real devices.

phase transitions | charge density wave | in situ electron microscopy | 4D-STEM | machine

Electronic phase transitions in quantum materials are of fundamental and technological interest, with potential applications ranging from quantum computers to next-generation microelectronics (1, 2). In a wide range of phase transitions, ranging from ice formation (3) to melt-crystallization cycles of phase change memories (4) to solid-solid structural transitions (5, 6), a materials microstructure—its defects, interfaces, surfaces, confinement, etc.—strongly influences the phase transition (7). However, the coupling of microstructure with electronic phase transitions in quantum materials is underexplored, despite huge implications for future devices. Bridging this gap requires real-space visualization to locally connect electronic phases with microstructural features during phase transitions. Such experiments are commonly performed with scanning probe microscopy, e.g., scanning tunneling microscopy (STM) or magnetic force microscopy, but these methods are surface sensitive and thus cannot access any subsurface (bulk) transformation process or defect (8, 9). Four-dimensional scanning transmission electron microscopy (4D-STEM) is a relatively new characterization method which averages the sample structure through thickness and, in principle, can simultaneously image quantum phases and microstructural defects with nanoscale spatial resolution (10). Processing and interpreting 4D-STEM datasets is difficult given massive dataset sizes (terabyte scale) and the need to extract subtle features from high-dimensional noisy data. Application of machine learning (ML) is a promising route to solve these issues (11, 12).

Here, using 4D-STEM with in situ cryogenic cooling, in situ electric biasing, and unsupervised ML, we directly visualize a dislocation-mediated quantum phase transition in 1T-TaS<sub>2</sub>. Specifically, we study the concomitant charge density wave (CDW) and insulatorto-metal transition in TaS<sub>2</sub>, and we show that basal dislocations (stacking solitons) both nucleate and pin the CDW transition. As a consequence, we show that the local dislocation density can modulate the nominal CDW transition temperature  $T_c$  by ~75 K, which is crucial for practical device applications. Moreover, a series of resistive transitions are realized in a single device, due to discrete jumps of the CDW phase boundary between dislocations. Such behavior is relevant to multistate memory devices. As basal dislocations are pervasive in layered materials (13), many quantum materials may similarly be affected by the dislocation density. Finally, our approach of in situ cryo-4D-STEM with electric biasing and ML provides real-space visualization of complex structure-property relations during phase transitions, an essential step for the engineering of quantum materials and devices.

## **Significance**

Quantum materials are of fundamental interest and are promising for applications such as next-generation computers. These materials are commonly studied with bulk averaging probes and thus their nanoscale properties are poorly understood. Here, using transmission electron microscopy with in situ cryogenic temperature control and electric biasing, we image a charge density wave (CDW) transition in 1T-TaS<sub>2</sub>. By correlating the device resistance, CDW phase, and the material microstructure, we show that basal dislocations—which are ubiquitous in 2D materials—both nucleate and pin the CDW transition. We then show how the dislocation density can be used to engineer device properties. Our work uses nanoscale cryogenic electron microscopy with machine learning to better understand quantum materials, a necessary step toward real-world devices.

Author contributions: J.L.H., H.P., L.F.K., E.-A.K., and J.J.C. designed research; J.L.H., H.P., S.S., N.S., K.M., and S.X. performed research; J.L.H., H.P., and K.M. analyzed data; and J.L.H., H.P., and J.J.C. wrote the paper.

The authors declare no competing interest.

This article is a PNAS Direct Submission.

Copyright © 2024 the Author(s). Published by PNAS. This article is distributed under Creative Commons Attribution-NonCommercial-NoDerivatives License 4.0

<sup>1</sup>J.L.H. and H.P. contributed equally to this work.

<sup>2</sup>To whom correspondence may be addressed. Email:

This article contains supporting information online at https://www.pnas.org/lookup/suppl/doi:10.1073/pnas. 2402129121/-/DCSupplemental.

Published August 6, 2024.

#### **Results and Discussion**

1T-TaS<sub>2</sub> is a two-dimensional (2D) material that hosts several CDW phases (14–16). Each layer consists of edge-sharing TaS<sub>6</sub> octahedral units, and layers are nominally stacked in an AA fashion (Fig. 1A). The primary CDW distortion consists of 13 neighboring Ta atoms bunched together into a so-called Star of David (Fig. 1B). In the low temperature ground state, the stars crystallize in a long-range ordered phase commensurate (C) with the underlying atomic lattice (Fig. 1C). This is the insulating C phase. Above ~200 K, TaS<sub>2</sub> transitions to the metallic nearly commensurate (NC) phase. This phase consists of ordered domains with a characteristic domain size  $D_{NC}$ ~ 10 nm, separated by phase slips in the CDW order parameter, i.e., discommensurations (Fig. 1D) (14-16). The C to NC phase transition causes a large resistance change and can be triggered thermally or via an applied electric bias, making TaS2 highly promising for next generation electronic devices (17-20). Still, better control over the transition is needed, for instance, the ability to tune the transition temperature  $T_c$ , ideally to room temperature.

Prior attempts to visualize the CDW transition in real-space have faced experimental limitations. Optical imaging can differentiate the insulating and metallic regions of TaS2 (21-23); however, these approaches are only indirectly sensitive to the CDW order parameter and can suffer from poor (~500 nm) spatial resolution (22). Atomic-scale analysis of the CDW is possible with STM (16, 24–26), but STM is surface sensitive and thus blind to subsurface (bulk) transformation processes. Moreover, STM does not offer a sufficiently large field-of-view to track mesoscale domain behavior which occurs on µm length scales (21-23). For both optical and STM methods, the ability to observe sample microstructure, e.g., dislocations, is limited. Alternatively, our use of 4D-STEM allows the direct quantification of the CDW order parameter as well as the sample microstructure, with both nanoscale spatial resolution and  $\mu m$  scale field-of-view. As we show below, this approach allows deep insight into the TaS2 phase transition and its coupling to atomic-scale defects.

Our experimental set-up and in situ 4D-STEM methodology are demonstrated in Fig. 1  $E\!-\!H$ . We first exfoliated a TaS<sub>2</sub> flake ( $\sim$ 60

nm thick, purchased from 2D Semiconductors) in an Ar glovebox and then transferred the flake to an in situ TEM chip (27, 28), which allows resistance measurements and temperature control from ~100 to 1,000 K within the STEM. The flake is imaged optically in Fig. 1E and within the STEM in Fig. 1F. With 4D-STEM, a converged electron probe (~14 nm full width at half maximum in our case) is rastered across the sample, and a diffraction pattern is recorded at each spatial coordinate. For this flake, we use a 4D-STEM scan size of 400 × 180 real-space pixels (21 nm pixel size), and an example diffraction pattern is shown in Fig. 1G. To study the CDW phase transition, we cooled the flake down to 120 K, and then slowly warmed the flake while collecting electrical resistance and 4D-STEM datasets every few K. The electrical resistance versus temperature (R vs. T) data shows a clear insulator-to-metal transition at ~200 K (Fig. 1H), and select snapshots from the 4D-STEM scans confirm the C to NC phase transition (Fig. 1 H, Insets). In the diffraction data, the brightest spots are Bragg diffraction spots, and the weaker spots are CDW satellite peaks (15, 19). In the C phase, the 1st and 2nd order CDW spots have equal intensity, while in the NC phase, the 1st order CDW spot intensities are greatly diminished (Fig. 11) (19). Additionally, there are slight modulations in the CDW angle  $\phi$  and wavevector magnitude k.

To quantify the CDW structure in real-space, we extract the domain size  $D_{NC}$  from the 4D-STEM diffraction data. To do so, we determine the position of every Bragg and CDW peak for each diffraction pattern, and then calculate the local CDW vector magnitude k and angle  $\varphi$  (see *SI Appendix*, Supplementary Note 1 for details). We then use the equation introduced by Thomson et al. (16) to determine the CDW domain size

$$D_{NC} = a/\sqrt{(2\pi\Delta\phi/360)^2 + (\Delta k/k_C)^2},$$
 [1]

where a is the atomic lattice parameter, and  $\Delta \varphi$  and  $\Delta k$  are the differences in  $\varphi$  and k relative to their C values,  $\varphi_c = 13.9^\circ$  and  $k_c = 13^{-1/2} a^* = 0.2773 a^*$ . Thus,  $D_{NC}$  acts as a single order parameter to differentiate the C and NC phases, with  $D_{NC} \to \infty$  for the C phase and  $D_{NC} \sim 10$  nm within the NC phase.

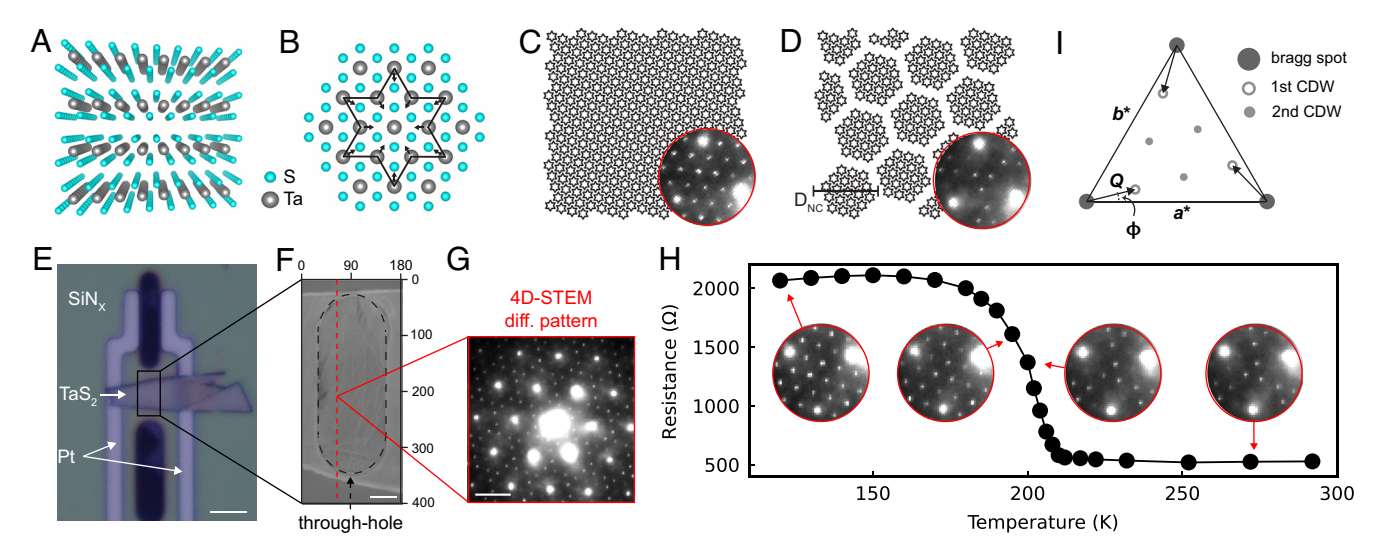


**Fig. 1.** Structure of 1T-TaS<sub>2</sub> and experimental methodology. (A and B) TaS<sub>2</sub> atomic structure shown in cross-section and plan-view, respectively, along with the Star of David distortion. (C and D) Cartoon schematics of the C and NC CDW phases, respectively, with corresponding electron diffraction data. For the NC phase, the domain size  $D_{NC}$  is shown. The TaS<sub>2</sub> flake is imaged optically (E) and within the STEM (P). The scale bars are 10 and 1  $\mu$ m in E and E, respectively. The tick marks on the STEM image indicate the pixel indices for the 4D-STEM datasets. 4D-STEM analysis was performed over the through-hole in the SiN<sub>x</sub> membrane. (G) Individual diffraction pattern extracted from a 4D-STEM scan taken at 200 K. (Scale bar, 3 nm<sup>-1</sup>.) (E) The electrical resistance measured during an in situ 4D-STEM experiment upon warming. *Insets* show diffraction data extracted from 4D-STEM scans. (E) Schematic of the diffraction data, showing the Bragg spots, 1st and 2nd order CDW spots, and the CDW angle E.

Fig. 2A and Movie S1 present the D<sub>NC</sub> maps at select temperatures upon warming; nonuniform nanoscale domain behavior is observed. At 120 K in the insulating phase, the measured  $D_{NC}$  is mostly > 100 nm. Within our measurement sensitivity,  $D_{NC}$  ~ 100 nm is consistent with the C phase (SI Appendix, Supplementary Notes 2 and 3). At 185 K, right as the flake resistance begins to drop (Fig. 1H), sharp lines appear in the  $D_{NC}$  map, with values of  $D_{NC}$  ~50 nm, indicating a local (partial) transition to the NC phase. The number of lines in the D<sub>NC</sub> map increases upon warming to 190 K and then to 195 K. Additionally, there is a small circular domain near the center of the through-hole with  $\boldsymbol{D}_{NC}$ ~16 nm at 185 K. From 195 to 204 K, the NC domain quickly grows to encompass the entire field-of-view. With further warming to 250 K, there is a homogenous decrease in  $D_{NC}$  across the entire flake, and there are no longer any well-defined features (lines, domains, etc.) in the CDW structure. The phase transition characteristics captured in Fig. 2 were not previously observed in any STM, optical, or other real-space analysis of the TaS<sub>2</sub> CDW transition, highlighting the benefits of the in situ cryo-4D-STEM approach.

We posit that the sharp lines and the circular domain observed in the  $D_{NC}$  maps (Fig. 2A) are connected to the flake's microstructure. To test this hypothesis, we generate a virtual image from the 4D-STEM data by summing the intensity of all Bragg diffraction spots (Fig. 2B). This image—based on Bragg diffraction contrast—reflects the structure of the underlying atomic crystal, as opposed to the CDW structure. The Bragg contrast image clearly shows a network of line defects (referred to as atomic defects for now) encompassing the entire field-of-view, and there is a direct correspondence between the atomic defects and the CDW C to NC evolution observed in the D<sub>NC</sub> maps. Moreover, we find that two atomic defects intersect at the circular domain in the D<sub>NC</sub> map (see the white arrow in Fig. 2B), suggesting again that the atomic defects are linked to the domain nucleation. We note that the presence of the line defects does not hinder our measurement of the CDW structure, as explained in SI Appendix, Supplementary Note 4. We conclude that the CDW phase transition is intimately connected to the flake microstructure.

To identify the exact nature of the atomic defects, we perform atomic-resolution imaging via high angle annular dark field (HAADF) STEM. For these measurements we study a much thinner flake (~20 nm) which is more amenable to atomic-resolution analysis (all studied TaS2 flakes (over a dozen) show similar defect structures, as evidenced with low magnification STEM imaging). Fig. 3A shows a low magnification HAADF-STEM image, revealing several line defects, similar to the ones shown in Fig. 2B. Fig. 3B presents a magnified view of one defect, which runs along the ~[1-10] direction. On either side of the defect, the atomic image reflects the projected Ta sublattice of 1T-TaS2 with AA stacking, as expected (the S sublattice is essentially invisible with HAADF-STEM). However, at the defect, two distinct Ta sublattices are observed, offset by a vector of ½ a. This image contrast is consistent with a basal dislocation having a Burgers vector along [100] and a line vector of  $\sim$ [1–10]. The experimental image contrast (Fig. 3C) is accurately reproduced via STEM image simulations (Fig. 3D) (29) of a basal dislocation, with the dislocation structure schematically shown in Fig. 3E. At the dislocation core, the layer stacking arrangement changes from the equilibrium AA structure, yielding two offset Ta sublattices in the projected STEM image. Analysis of the adjacent line defects in Fig. 3A is also consistent with basal dislocations, albeit with different Burgers vectors (SI Appendix, Fig. S1). Reexamining the 4D-STEM data in

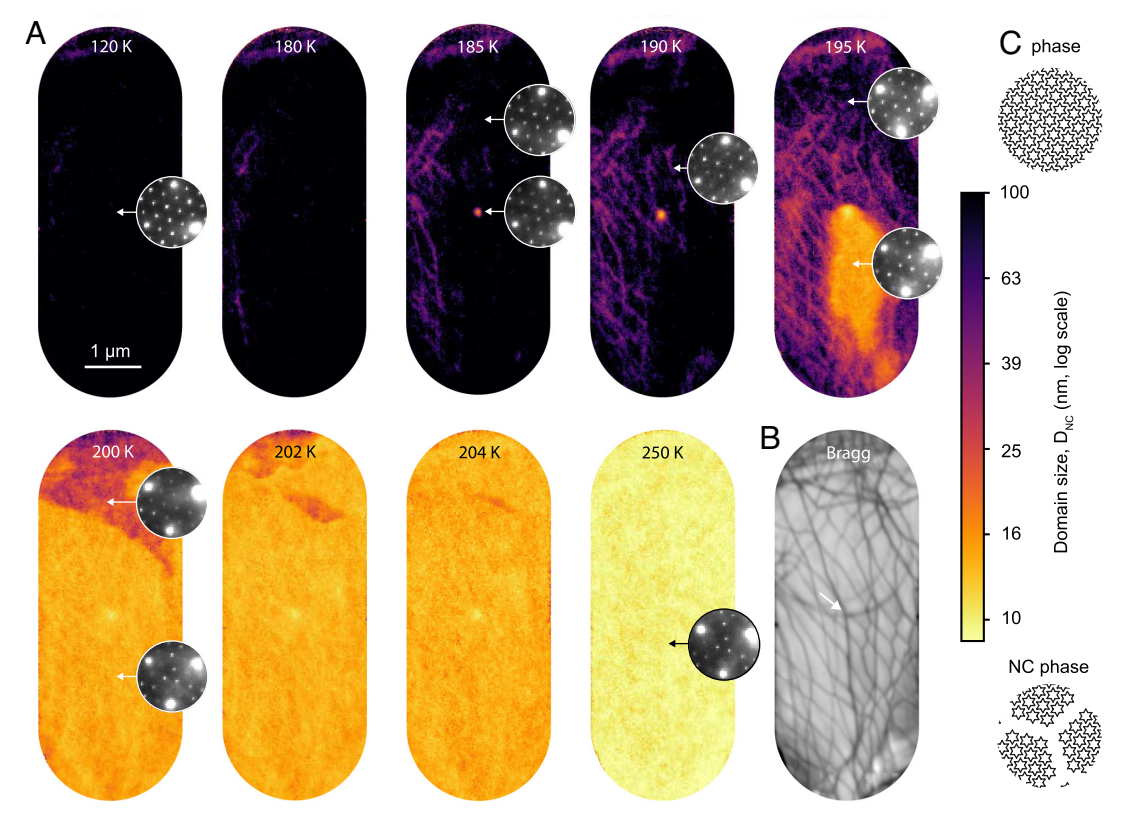
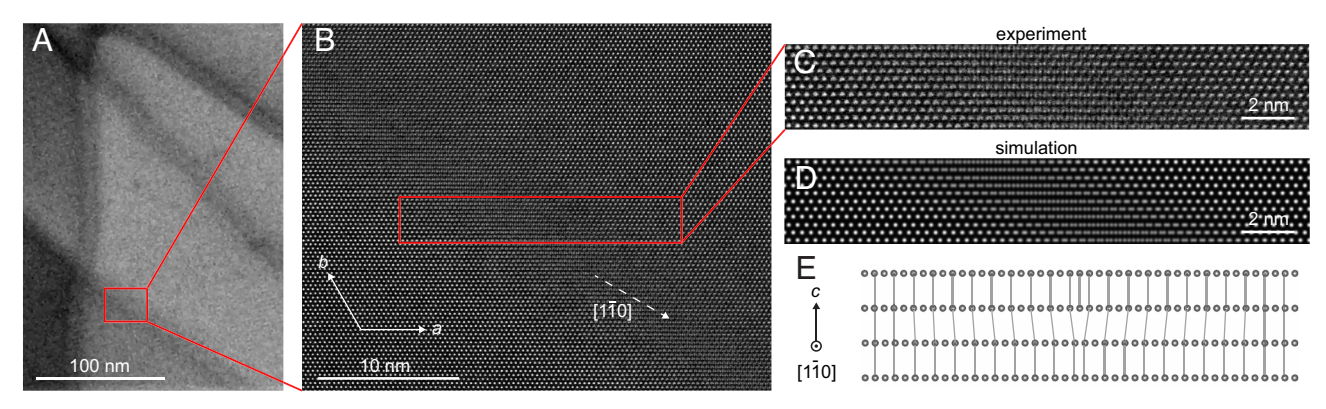


Fig. 2. Real-space visualization of the CDW phase transition. (A) 4D-STEM derived maps of the CDW domain size  $D_{NC}$  for select temperatures. The data are  $cropped \ to \ the \ through-hole \ in \ the \ SiN_x \ membrane; see \ Fig. \ 1F. \ Note \ that \ the \ 4D-STEM \ data \ were \ acquired \ during \ the \ same \ warming \ cycle \ used \ to \ generate \ the \ acquired \ the \ through-hole \ in \ the \ SiN_x \ membrane; see \ Fig. \ 1F. \ Note \ that \ the \ 4D-STEM \ data \ were \ acquired \ during \ the \ same \ warming \ cycle \ used \ to \ generate \ the \ through-hole \ in \ the \ SiN_x \ membrane; see \ Fig. \ 1F. \ Note \ that \ the \ 4D-STEM \ data \ were \ acquired \ during \ the \ same \ warming \ cycle \ used \ to \ generate \ the \ through-hole \ in \ through-hole \ through-hole \ in \ through-ho$ R vs. T data in Fig. 1H. Insets show local diffraction data. (B) Virtual STEM image generated by summing the intensity of every Bragg diffraction beam. Data were collected at 195 K. The white arrow in B marks the location of the small circular CDW domain first observed at 185 K in A.



**Fig. 3.** Atomic resolution imaging of basal dislocations. (*A*) Low magnification HAADF-STEM image of a thin  $TaS_2$  flake in plan-view (the ab-plane) showing several line defects. (*B*) Zoomed in region of (*A*) showing a line defect at atomic resolution. (*C*) Enlarged view of the line defect, with a corresponding STEM image simulation (*D*) along with the atomic model used to generate the STEM simulation (*E*). Only the Ta sublattice is shown.

Fig. 2*B*, the observed defect network is qualitatively similar to dislocation networks observed in both conventional 3D materials (30, 31) as well as 2D materials (13, 32–35) including  $TaS_2$  (36, 37). Hence, we conclude that the atomic defects observed with 4D-STEM are basal dislocations, which are expected in exfoliated 2D materials.

Our findings demonstrate that basal dislocations strongly influence the CDW phase transition in 1T-TaS2, and therefore, engineered dislocation structures may be used to control the CDW transition, e.g., by altering the  $T_c$ . To test this hypothesis, we study a second device, shown optically in the Fig. 4 A, Inset (flake thickness of ~65 nm). Initially, the flake displayed a well-defined insulator-to-metal transition upon warming, as expected (Fig. 4A black curve). Next, we repeatedly cycled the flake from 120 K up to 500 K and applied large voltage pulses [10 V across a 10 µm channel, with ~µs duration to avoid substantial heating (38)] with the intention of increasing the dislocation density (we assume dislocations can be formed via thermal- or voltage-induced strain). After cycling, the insulator-to-metal transition was split into series of discrete resistance drops, each with a  $T_c$  lower than the start (Fig. 4A, red curve). Additionally, virtual STEM imaging shows the presence of dislocations, with a high local concentration of dislocations indicated with the red arrow (Fig. 4B and SI Appendix, Fig. S2).

Given the complexity of dislocation networks in this flake, we apply unsupervised ML to cluster the 4D-STEM data collected upon warming. If our observation of the one-to-one correlation between dislocations and CDW domain nucleation (Fig. 2) is universal, then we expect that ML will cluster the CDW phase transition behavior in a way that can be mapped onto the spatial distribution of dislocations. We start with the X-TEC methodology—a ML approach we designed for the analysis of temperature-dependent X-ray diffraction using Gaussian mixture model based clustering (39–41)—and we adopt this method to temperature-dependent 4D-STEM analysis. Our approach largely ignores the complexities of individual diffraction patterns, and instead focuses on how the diffraction data evolve with temperature. This strategy improves robustness of the XTEC clustering against measurement noise and sample tilt.

The ML approach is outlined in Fig. 4 *C–E* and discussed in detail in *Materials and Methods* and *SI Appendix*, Supplementary Note 5. To begin, each diffraction pattern is segmented according to the Bragg diffraction spots, dividing the diffraction pattern into half Brillouin zone (BZ) triangles (Fig. 4*C*). Next, CDW spots above the background noise level are identified with a peak finding algorithm, and the number of CDW spots per half BZ are

calculated,  $N_{\rm CDW}$ . Note that in principle,  $N_{\rm CDW}$  = 6 for the C phase, and  $N_{\rm CDW}$  = 3 for the NC phase (Fig. 1 C and D). By extracting  $N_{\rm CDW}$  from each diffraction pattern, we reduce the 5D dataset (temperature, real space x and y, momentum space  $k_x$  and  $k_y$ ) to a 3D dataset (temperature, real space x and y). Next, we use the Gaussian mixture model (42) to cluster the data in real space based on the thermal evolution of  $N_{\rm CDW}$  (Materials and Methods). We used the Elbow method (43) to determine the optimal number of clusters (4), see SI Appendix, Fig. S3.

Fig. 4D shows the real space map of the clustering results, where the different clusters are interpreted as regions of the flake showing distinct CDW behavior. Fig. 4E plots the mean  $N_{\rm CDW}$  versus temperature for each of the clusters, where abrupt changes in  $N_{\rm CDW}$  are interpreted as local CDW phase transitions. The real space cluster map (Fig. 4D) shows excellent agreement with the dislocation structures observed in the virtual STEM image (Fig. 4B). In particular, the region of cluster 0 (blue region) coincides with the region of high dislocation density, as marked with the red arrows in Fig. 4 B and D. Supporting our claim that dislocations nucleate the metallic NC phase, cluster 0 shows the C to NC phase transition at the earliest temperature of ~155 K (Fig. 4E). Conversely, clusters 1 to 3 (yellow, orange, and pink) show the most pronounced transition at ~190 K (Fig. 4E), and these regions do not contain as many dislocations as cluster 0. Additionally, ML analysis provides a real-space explanation for the multiple resistance steps observed in Fig. 4A. Specifically, each cluster shows distinct transition temperature(s) which collectively explain the multiple device resistance jumps. The resistance drop at 155 K is explained by CDW transitions in cluster 0 and 1; the resistance drop at 190 K is explained by CDW transitions in clusters 2 and 3 (and to a lesser extent 0 and 1); and the resistance drop at 220 K is explained by CDW transitions in clusters 1 and 2 (Fig. 4E). Thus, ML analysis allows us to establish a microscopic picture for the resistance, with each resistance step corresponding to spatially separate CDW transitions, which supports our hypothesis that a high concentration of dislocations can strongly influence the CDW  $T_c$ .

To supplement the ML cluster analysis, we map  $D_{\rm NC}$  in real-space and present maps from select temperatures (Fig. 4*G*). At T=150 K, much of the flake is in the C phase; however, at the region of increased dislocation density (which roughly coincides with cluster 0), we observe a suppressed  $D_{\rm NC}$  of ~16 nm. The same CDW structure is observed down to the lowest measured temperature of 130 K. This finding indicates that a high concentration of dislocations can suppress the C phase, at least for temperatures down to 130 K, ~75 K below the nominal  $T_c$ . With increasing temperature, the NC domain centered at cluster 0 grows,

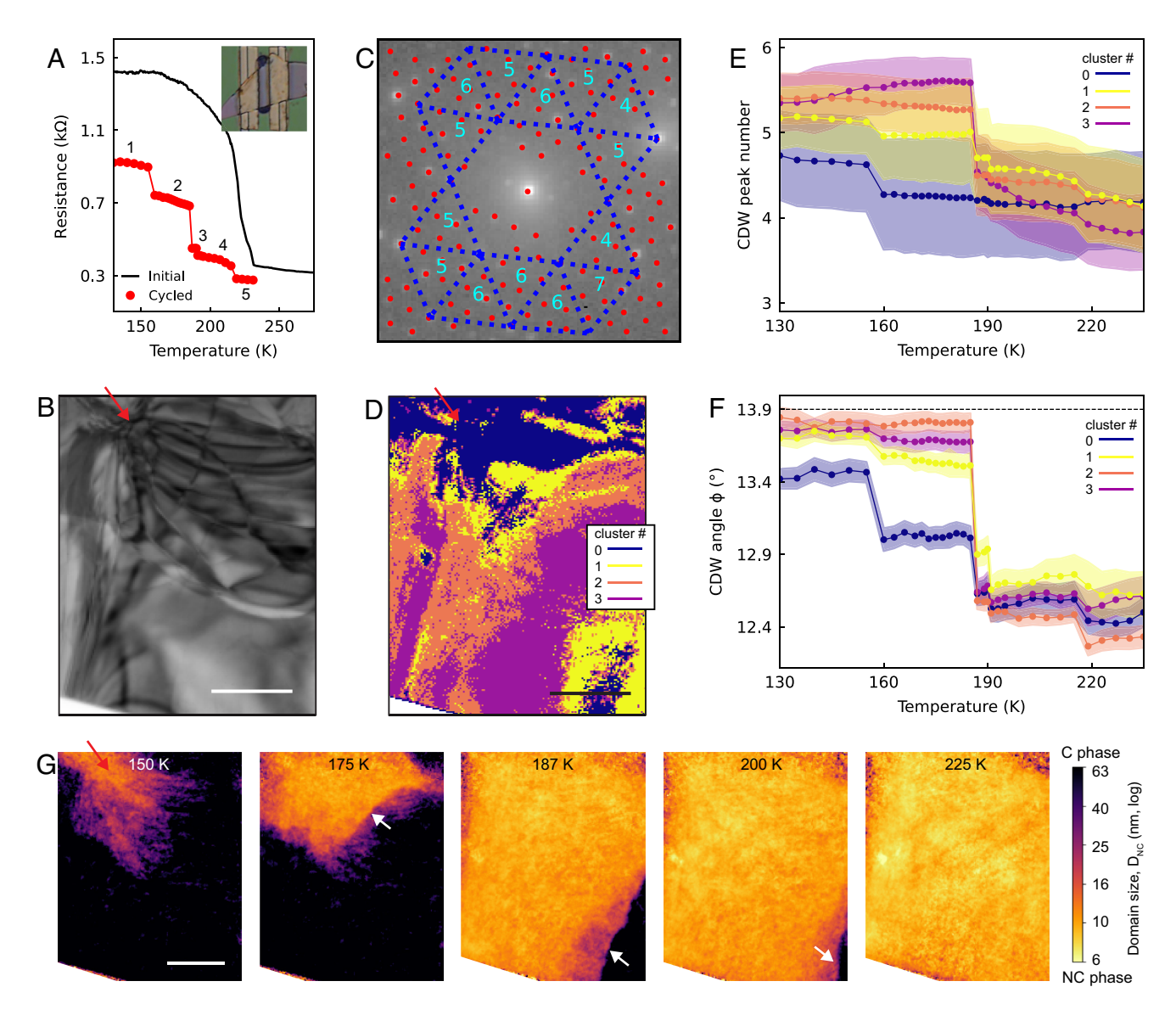


Fig. 4. ML analysis of 4D-STEM during phase transition. (A) R vs. T for a TaS<sub>2</sub> flake (pictured in the *Inset*, 80 × 80  $\mu$ m field of view), both in the initial state and after temperature and electric field cycling. For the cycled R vs. T data, each of the resistance plateaus are labeled. (B) Virtual STEM image generated from the 4D-STEM data. The red arrow marks a region of high dislocation density. (Scale bar, 1 μm.) (C) Example diffraction pattern from the 4D-STEM dataset, with the ML preprocessing steps shown. Dashed blue lines divide the data into half-BZs, and red dots mark diffraction spots identified with the peak finding algorithm. For each half-BZ, the number of CDW peaks is listed,  $N_{\text{CDW}}$ . (D) Real-space visualization of the four clusters determined from the ML analysis. (Scale bar, 1  $\mu$ m.) (E) The average number of CDW peaks for each cluster, N<sub>CDW</sub>, determined from the ML analysis. The plot is color-coded according to the cluster labels shown in the panel. The lines show the mean, and the shaded area represents the SD of the trajectories in that cluster. (F) Average CDW angle  $\phi$  for each of the clusters as a function of temperature. The lines show the mean, and shading shows the SD of the values of  $\phi$  in the cluster. (G) CDW domain size  $D_{NC}$  as a function of temperature, showing different domain structures after each resistance jump. The five presented temperatures correspond to the five resistance plateaus labeled in A. (Scale bar, 1 μm.) The white arrows mark the positions of dislocations that pin the CDW phase boundary (SI Appendix, Fig. S2). The red arrow shows the region of high dislocation density.

eventually encompassing the entire flake. Critically, the  $D_{NC}$  maps show that for each of the abrupt changes in electrical resistance, there is a discrete expansion of the NC phase. This process is mediated by the dislocation network. The domain boundary separating the NC and C phases preferentially lies along dislocation lines, and the domain boundary jumps from one dislocation to the next during domain growth. White arrows mark the dislocation lines which pin the domain boundary (Fig. 4G). Hence, the discrete insulator-to-metal transitions reflected in the R vs. T curve are attributed to sudden expansion of the NC phase volume fraction, as the CDW domain boundary jumps between dislocations.

Last, we average the diffraction data in real-space according to the ML assigned clusters, which provides temperature-dependent diffraction data for each of the four clusters. We then process these

data to extract the CDW angle for each cluster, as shown in Fig. 4F. Initially, for T < 155 K, clusters 1 to 3 all show  $\phi \sim 13.9^{\circ}$ , consistent with the C phase. In contrast, cluster 0 shows  $\phi \sim 13.5^{\circ}$ , indicating that cluster 0 never fully entered the C phase, in agreement with our maps of D<sub>NC</sub> (Fig. 4G). With increasing temperature, the CDW transitions identified in the  $N_{\text{CDW}}$  plots are all reproduced in the CDW angle  $\phi$  (Fig. 4 E and F), verifying our ML methodology based on  $N_{\text{CDW}}$ . The SD (see shaded regions) of  $\phi$  are much less than that of  $N_{\text{CDW}}$ ; this is because sample tilt will alter the diffraction spot intensities and thus  $N_{\rm CDW}$ , but tilt does not influence the diffraction spot positions, which determine  $\phi$ .

We propose two microscopic mechanisms through which the dislocations may interact and influence the CDW. First, the C and NC phases have different out-of-plane structure: the C CDW forms out-of-plane dimers, which lack long-range coherence along  $\boldsymbol{c}$ , while the NC CDW has a well-defined three-layer stacking along  $\boldsymbol{c}$  (44, 45). Thus, it is possible that the local change in layer stacking at basal dislocations (which are commonly referred to as stacking solitons) couples to the CDW energetics. Alternatively, large in-plane strains are expected around the dislocation core. Due to the strong coupling between the atomic lattice and CDW structure in TaS<sub>2</sub> (46, 47), it is reasonable to expect that large strain may influence the CDW transition thermodynamics and kinetics. We cannot directly verify this hypothesis with our experimental geometry, because plan-view strain measurements average together the compensating compressive and tensile strains expected above and below basal dislocations. First principles calculations may help elucidate the underlying coupling between dislocations and CDW behavior.

### **Conclusions**

We studied the prototypical CDW and insulator-to-metal transition in 1T-TaS<sub>2</sub> and found that basal dislocations can i) nucleate the phase transition, ii) pin CDW domain boundaries, and iii) given a sufficient concentration, suppress the C phase. Based on these observations, we directly identify coupling between a CDW phase transition and the local microstructure in real space. We expect the impact of dislocations on CDWs to be widespread, given that basal dislocations have been identified in a large number of 2D materials, both for flakes on holey TEM grids and flakes exfoliated onto conventional substrates (e.g., SiO<sub>2</sub> and h-BN) (13, 32-37, 48). However, it is unclear how factors such as the flake thickness, exfoliation method, and substrate may influence dislocation networks, and, in turn, CDW properties. Answering these questions may enable dislocation-engineering of TaS<sub>2</sub> for specific device functionality. Indeed, the TaS2 CDW shows a complex thickness-dependent behavior (18, 19, 49, 50), which may be linked to thickness-dependent dislocation structures. A much finer control over the dislocation structure (and thus the CDW) may also be achieved by electric-field control of individual dislocations, as demonstrated in certain materials (51, 52). Dislocations are also known to have a nontrivial influence on superconductivity (53), though it is unclear what role dislocations may play in systems with competing superconducting and CDW orders, e.g.,  $1\text{T-TaS}_2$  and the high  $T_c$  cuprates (54). In principle, liquid He cryo-STEM could reveal such effects, if present. Last, our method of combining in situ cryo-4D-STEM with in situ transport and ML analysis is a promising approach to study structure-property coupling in other quantum materials during phase transitions.

#### **Materials and Methods**

4D-STEM measurements were performed with a Thermo Fisher Titan Themis 60 to 300 kV instrument, operated at 120 kV. The 4D-STEM datasets were captured using an EMPAD-G2 detector, the beam current was  $\sim$ 1.5 nA, and the convergence semi-angle was set to 0.15 mrad, providing a real-space probe size of  $\sim$ 14 nm. The pixel dwell time was 2 ms. To extract the D<sub>NC</sub> maps from the 4D-STEM data, we followed the procedures described in ref. 38 and explained in *SI Appendix*, Supplementary Note 1. We used the HennyZ in situ holder (model FDCHB-6) (28), with heating and biasing nanochips purchased from DENS Solutions (part # DS-PT.2B4H.DS-1).

- 1. X. Liu, M. C. Hersam, 2D materials for quantum information science. Nat. Rev. Mater. 4, 669–684 (2019).
- D. N. Basov, R. D. Averitt, D. Hsieh, Towards properties on demand in quantum materials. Nat. Mater. 16, 1077-1088 (2017)
- 3. C. A. Angell, Supercooled water. Annu. Rev. Phys. Chem. 34, 593–630 (1983).
- P. Nukala, C.-C. Lin, R. Composto, R. Agarwal, Últralow-power switching via defect engineering in germanium telluride phase-change memory devices. Nat. Commun. 7, 10482 (2016).
- R. Lopez, T. E. Haynes, L. A. Boatner, L. C. Feldman, R. F. Haglund, Size effects in the structural phase transition of VO<sub>2</sub> nanoparticles. *Phys. Rev. B* 65, 224113 (2002).

For the temperature-dependent 4D-STEM scans, each scan took several minutes to complete, and then the temperature was adjusted at a rate of 1 K/s. For the atomic-resolution imaging in Fig. 3, we used a 5th-order probe-corrected Thermo Fisher Spectra operated at 200 kV with a convergence semiangle of 30 mrad.

For the STEM image simulation in Fig. 3, we used the COMPUTEM package (29). We used the INCOSTEM method, which projects the 3D supercell potential to 2D, and then convolves the potential with the probe point spread function to form an image.

In producing Fig. 4, we adopted an unsupervised ML algorithm, where the feature extraction is performed by counting the number of CDW spots in the Bragg diffraction pattern in momentum space as shown in Fig. 4C. We improve the original method used in X-TEC by using a more robust quantity against tilting and misalignment. We first detect all the Bragg diffraction spots, and connect the neighboring ones to triangularize the momentum space, where each triangle corresponds to half BZ, as shown in Fig. 4C. We then count the average number of CDW spots in one diffraction pattern at a fixed temperature, and then change to another temperature to track the thermal trend at each real space position. Finally, we treat the thermal trend at each real space position as a high-dimensional vector, and perform the Gaussian mixture model to cluster in the real space. Further details are provided in *SI Appendix*, Supplementary Note 5 (55).

An unknown parameter in this procedure is the number of distinctive clusters, which needs to be determined before running the clustering algorithm. Therefore, we run the same algorithm with different numbers of clusters, and compare the clustering performance using the Bayesian information criterion (a measure to quantify the fit of a model to the data, a lower value generally indicates a better fit) as shown in *SI Appendix*, Fig. S3. To determine the optimal number of clusters, we use the heuristic Elbow method to look for the "kink" (the most significant drop before the change becomes marginal).

Data, Materials, and Software Availability. Machine learning analysis and datasets have been deposited in PARADIM Data (10.34863/0k5x-w691) (55).

**ACKNOWLEDGMENTS.** The in situ four-dimensional scanning transmission electron microscopy and machine learning analysis were supported by the Department of Energy, Basic Energy Sciences DE-SC0023905. The computation was carried out on the cluster supported by the Gordon and Betty Moore Foundation's Emergent Phenomena in Quantum Systems Initiative, Grant GBMF10436 to Eun-Ah Kim. N.S. acknowledges support from the NSF Graduate Research Fellowships Program under Award No. DGE-2139899. H.P. was supported by the NSF [platform for the accelerated realization, analysis, and discovery of interface materials (PARADIM)] under Cooperative Agreement No. DMR-2039380. K.M. was supported by Eric and Wendy Schmidt AI in Science Postdoctoral Fellowship: A Schmidt Futures program. Device fabrication was performed in part at the Cornell NanoScale Facility, a member of the National Nanotechnology Coordinated Infrastructure, which is supported by the NSF (Grant NNCI-2025233). This work made use of the electron microscopy facility of PARADIM, which is supported by the NSF under Cooperative Agreement No. DMR-2039380, and the Cornell Center for Materials Research Shared Facilities which are supported through the NSF Materials Research Science and Engineering Centers Program (DMR-1719875). The Titan Themis 300 was acquired through NSF-MRI-1429155, with additional support from Cornell University, the Weill Institute and the Kavli Institute at Cornell.

Author affiliations: \*Department of Materials Science and Engineering, Cornell University, Ithaca, NY 14853; \*Department of Physics, Cornell University, Ithaca, NY 14853; \*School of Applied and Engineering Physics, Cornell University, Ithaca, NY 14853; \*dKavli Institute at Cornell for Nanoscale Science, Cornell University, Ithaca, NY 14853; and \*Department of Physics, Ewha Womans University, Seoul 03760, South Korea

- A. Kwiatkowski da Silva et al., Phase nucleation through confined spinodal fluctuations at crystal defects evidenced in Fe-Mn alloys. Nat. Commun. 9, 1137 (2018).
- 7. D. R. Gaskell, Introduction to the Thermodynamics of Materials (CRC Press, 2008).
- 8. K. A. Moler, Imaging quantum materials. *Nat. Mater.* **16**, 1049–1052 (2017).
- J. L. Hart, J. J. Cha, Seeing quantum materials with cryogenic transmission electron microscopy. Nano Lett. 21, 5449-5452 (2021).
- C. Ophus, Four-Dimensional scanning transmission electron microscopy (4D-STEM): From scanning nanodiffraction to ptychography and beyond. *Microsc. Microanal.* 25, 563–582 (2019).

- 11. S. R. Spurgeon et al., Towards data-driven next-generation transmission electron microscopy. Nat. Mater. 20, 274-279 (2021).
- S. V. Kalinin et al., Machine learning in scanning transmission electron microscopy. Nat. Rev. Methods Prim. 2, 11 (2022).
- S. Amelinckxa, P. Delavignette, Observation of dislocations in non-metallic layer structures. Nature 185. 603-604 (1960).
- J. Wilson, F. Di Salvo, S. Mahajan, Charge-density waves and superlattices in the metallic layered transition metal dichalcogenides. *Adv. Phys.* **24**, 117–201 (1975).
- T. Ishiguro, H. Sato, Electron microscopy of phase transformations in 1T-TaS<sub>2</sub>. Phys. Rev. B 44, 2046-2060 (1991).
- R. E. Thomson, B. Burk, A. Zettl, J. Clarke, Scanning tunneling microscopy of the charge-density-wave structure in 1T-Ta<sub>2</sub>. *Phys. Rev. B* **49**, 16899–16916 (1994).
- M. J. Hollander et al., Electrically driven reversible insulator-metal phase transition in 1T-TaS<sub>2</sub>. Nano Lett. 15, 1861-1866 (2015).
- M. Yoshida, R. Suzuki, Y. Zhang, M. Nakano, Y. Iwasa, Memristive phase switching in twodimensional 1T-TaS<sub>2</sub> crystals. Sci. Adv. 1, 1-7 (2015).
- A. W. Tsen et al., Structure and control of charge density waves in two-dimensional 1T-TaS<sub>2</sub>. Proc. Natl. Acad. Sci. U.S.A. 112, 15054-15059 (2015).
- I. Vaskivskyi et al., Fast electronic resistance switching involving hidden charge density wave states.
- Nat. Commun. 7, 11442 (2016). 21. A. J. Frenzel et al., Infrared nanoimaging of the metal-insulator transition in the charge-density-
- wave van der Waals material 1T-Ia5*2, Phys. Rev. B* **97**, 035111 (2018).

  T. Patel *et al.*, Photocurrent imaging of multi-memristive charge density wave switching in twodimensional 1T-TaS<sub>2</sub>. Nano Lett. 20, 7200-7206 (2020).
- S. S. Zhang et al., Nano-infrared imaging of metal insulator transition in few-layer 1T-TaS<sub>2</sub>.
- Nanophotonics 12, 2841-2847 (2023). S. M. Walker et al., Observation and manipulation of a phase separated state in a charge density
- wave material. Nano Lett. 22, 1929-1936 (2022). 25. K. Bu *et al.*, Possible strain induced Mott gap collapse in 1T-TaS<sub>2</sub>. *Commun. Phys.* **2**, 146 (2019).
- Y. Geng et al., Hysteretic electronic phase transitions in correlated charge density wave state of 1T-TaS<sub>2</sub>. Phys. Rev. B 107, 195401 (2023).
- 27. H. H. P. Garza et al., "MEMS-based sample carriers for simultaneous heating and biasing experiments: A platform for in-situ TEM analysis" in 2017 19th International Conference on Solid-State Sensors, Actuators and Microsystems (TRANSDUCERS) (IEEE, 2017), pp. 2155-2158, 10.1109/ TRANSDUCERS.2017.7994502.
- B. H. Goodge, E. Bianco, N. Schnitzer, H. W. Zandbergen, L. F. Kourkoutis, Atomic-resolution Cryo-STEM across continuously variable temperatures. Microsc. Microanal. 26, 439-446 (2020).
- E. J. Kirkland, Advanced Computing in Electron Microscopy (Springer US, 2010).
- S. B. Samavedam, E. A. Fitzgerald, Novel dislocation structure and surface morphology effects in relaxed Ge/Si-Ge(graded)/Si structures. J. Appl. Phys. 81, 3108-3116 (1997).
- A. Sakai, N. Taoka, O. Nakatsuka, S. Zaima, Y. Yasuda, Pure-edge dislocation network for strainrelaxed SiGe/Si(001) systems. Appl. Phys. Lett. 86, 1-3 (2005).
- D. L. Medlin, N. Yang, C. D. Spataru, L. M. Hale, Y. Mishin, Unraveling the dislocation core structure at a van der Waals gap in bismuth telluride. Nat. Commun. 10, 1820 (2019).

- 33. K. Ko et al., Operando electron microscopy investigation of polar domain dynamics in twisted van der Waals homobilayers. Nat. Mater. 22, 992-998 (2023).
- P. Denninger, P. Schweizer, C. Dolle, E. Spiecker, Diffraction contrast analysis of dislocations in 2D materials using true dark-field and 4D-STEM in SEM. Microsc. Microanal. 27, 1816-1819 (2021).
- J. H. Kim et al., Interface-driven partial dislocation formation in 2D heterostructures. Adv. Mater. 31,
- R. Hovden et al., Atomic lattice disorder in charge-density-wave phases of exfoliated dichalcogenides (1T-TaS<sub>2</sub>). Proc. Natl. Acad. Sci. U.S.A. **113**, 11420-11424 (2016).
- R. Hovden et al., Thickness and stacking sequence determination of exfoliated dichalcogenides (1T-TaS<sub>2</sub>, 2H-MoS<sub>2</sub>) using scanning transmission electron microscopy. *Microsc. Microanal.* 24, 387-395 (2018).
- J. L. Hart et al., In operando cryo-STEM of pulse-induced charge density wave switching in TaS2. Nat. Commun. 14, 8202 (2023).
- K. Mallayya *et al.*, Bragg glass signatures in Pd\_ErTe<sub>3</sub> with X-ray diffraction temperature clustering (X-TEC). *Nat. Phys.* **20**, 822-829 (2024), 10.1038/s41567-023-02380-1.
- L. Kautzsch  $\it et\,al.$ , Structural evolution of the kagome superconductorsAV $_3$ Sb $_5$  (A = K, Rb, and Cs) through charge density wave order. Phys. Rev. Mater. 7, 024806 (2023).
- J. Venderley et al., Harnessing interpretable and unsupervised machine learning to address Big Data from modern X-ray diffraction. Proc. Natl. Acad. Sci. U.S.A. 119, 1-10 (2022).
- K. P. Murphy, Machine Learning: A Probabilistic Perspective (MIT Press, 2012).
- H. Humaira, R. Rasyidah, "Determining the appropiate cluster number using elbow method for Kmeans algorithm" in Proceedings of the 2nd Workshop on Multidisciplinary and Applications (WMA) (EAI, 2018), 10.4108/eai.24-1-2018.2292388.
- Q. Stahl et al., Collapse of layer dimerization in the photo-induced hidden state of 1T-TaS2. Nat. Commun. 11, 1247 (2020).
- S. Tanda, T. Sambongi, T. Tani, S. Tanaka, X-ray study of charge density wave structure in 1T-TaS<sub>2</sub>. *J. Phys. Soc. Japan* **53**, 476–479 (1984).
- O. Sezerman, A. M. Simpson, M. H. Jericho, Thermal expansion of 1T-TaS2 and 2H-NbSe2. Solid State Commun. 36, 737-740 (1980).
- S. S. Philip, J. C. Neuefeind, M. B. Stone, D. Louca, Local structure anomaly with the charge ordering transition of 1T-TaS2. Phys. Rev. B 107, 184109 (2023).
- J. L. Hart et al., Emergent layer stacking arrangements in c-axis confined MoTe<sub>2</sub>. Nat. Commun. 14, 4803 (2023).
- S. H. Sung et al., Two-dimensional charge order stabilized in clean polytype heterostructures. Nat. Commun. 13, 413 (2022).
- Y. Yu et al., Gate-tunable phase transitions in thin flakes of 1T-TaS2. Nat. Nanotechnol. 10, 270-276
- M. Yankowitz et al., Electric field control of soliton motion and stacking in trilayer graphere. Nat. Mater. 13, 786-789 (2014).
- M. Li et al., Harnessing dislocation motion using an electric field. Nat. Mater. 22, 958-963 (2023).
- M. Li et al., Tailoring superconductivity with quantum dislocations. Nano Lett. 17, 4604-4610 (2017).
- B. Sipos et al., From Mott state to superconductivity in 1T-TaS $_2$ . Nat. Mater. **7**, 960–965 (2008). J. L. Hart et al., Data from "Real-space visualization of a defect-mediated charge density wave transition". PARADIM Data. https://doi.org/10.34863/0k5x-w691. Deposited July 22, 2024.